

Laser-Arc Hybrid Welding of Dissimilar Titanium Alloy and Stainless Steel Using Copper Wire

MING GAO, CONG CHEN, LEI WANG, ZEMIN WANG, and XIAOYAN ZENG

Laser-arc hybrid welding with Cu3Si filler wire was employed to join dissimilar Ti6Al4V titanium alloy and AISI316 stainless steel (316SS). The effects of welding parameters on bead shape, microstructure, mechanical properties, and fracture behavior were investigated in detail. The results show that cross-weld tensile strength of the joints is up to 212 MPa. In the joint, obvious nonuniformity of the microstructure is found in the fusion zone (FZ) and at the interfaces from the top to the bottom, which could be improved by increasing heat input. For the homogeneous joint, the FZ is characterized by $\text{Fe}_{67-x}\text{Si}_x\text{Ti}_{33}$ dendrites spreading on α -Cu matrix, and the two interfaces of 316SS/FZ and FZ/Ti6Al4V are characterized by a bamboo-like 316SS layer and a CuTi_2 layer, respectively. All the tensile samples fractured in the hardest CuTi_2 layer at Ti6Al4V side of the joints. The fracture surface is characterized by river pattern revealing brittle cleavage fracture. The bead formation mechanisms were discussed according to the melt flow and the thermodynamic calculation.

DOI: 10.1007/s11661-015-2798-3

© The Minerals, Metals & Materials Society and ASM International 2015

I. INTRODUCTION

THE joining of dissimilar titanium (Ti) alloy and stainless steel (SS) is of interest for chemical and nuclear applications. Previous studies have shown that the joining of Ti alloy and SS suffers from two major challenges.^[1-4] One is the formation of brittle intermetallic compounds (IMCs) between Ti and Fe. The other is the occurrence of cracks and residual stresses that are caused by the great differences in thermal properties between Ti and SS. For example, the thermal expansion coefficients of Ti and SS are $8.4 \times 10^{-6} \text{ K}^{-1}$ and $16.6 \times 10^{-6} \text{ K}^{-1}$, respectively.

Considering the above difficulties, the interlayers such as Cu,^[5] Ag,^[6] Ni,^[7,8] Al,^[9] and Mg^[10] have been used to suppress the formation of Ti/Fe IMCs during welding. Among them, Cu would be a potential candidate to meet the needs of industry. Firstly, the melting point of Cu is higher than that of Al or Mg, denoting that the joint using Cu interlayer has better high-temperature performance. Besides, the melting point of Cu is not too high, which would be better to increase the adjustable range of welding parameters. Secondly, Cu is cheaper than Ag and Ni, which reduces the manufacturing costs. Thirdly and importantly, Cu does not form any IMCs with steel, although Cu-Ti binary phase diagram indicates the occurrence of Cu_2Ti , Cu_3Ti_2 , CuTi , and CuTi_2 with increasing Cu content. Kundu *et al.* found that the tensile strength of diffusion-bonded commercial pure Ti and 316SS was up to 318 MPa when Cu was used as the

interlayer.^[5] Similarly, Wang *et al.* found that the tensile strength of electron beam-welded dissimilar Ti15Al3V alloy and 316SS with Cu interlayer was up to 224 MPa.^[11] Refaey and Tillmann found that accepted diffusion-bonded pure Ti and mild steel was obtained in lap configuration by using Cu12Mn2Ni interlayer.^[1]

Nowadays, diffusion bonding/brazing has been one of the most common processes to join Ti alloy and SS. But it is impractical for mass production and needs great care in surface preparation. Friction stir welding (FSW) was employed to join dissimilar Ti alloy and SS recently.^[12,13] Although the results showed that the tensile strength of FSWed Ti/SS joint was up to 400 MPa, the high melting point of either steel or Ti alloy is a big challenge for long-term usage of stir pin. Being a high efficiency and flexibility technique, laser welding has made great achievements in joining dissimilar metals, such as Mg/steel,^[14] Mg/Ti,^[15] Al/Ti,^[16,17] Cu/steel,^[18] and Al/steel.^[19] For example, our previous study has demonstrated that Ti6Al4V/316SS joints of acceptable quality and properties can be obtained by fiber laser welding with Mg interlayer,^[10] and the cross-weld strength of the joints is up to 221 MPa. However, the Cu is seldom welded by pure laser welding because the high reflection of laser beam will reduce the process stability and efficiency dramatically. To avoid this problem, laser-arc hybrid welding is employed to join dissimilar Ti alloy and SS in this study.

As a focused research field, laser-arc hybrid welding has been paid a lot of attentions because of its superiorities inherited from laser and arc: high welding speed, stable process, desirable bead appearances, excellent mechanical properties, and good gap bridging ability.^[20] The previous studies have demonstrated that laser hybrid welding is an effective way to join dissimilar

MING GAO, Associate Professor, CONG CHEN and LEI WANG, Doctoral Students, ZEMIN WANG and XIAOYAN ZENG, Professors, are with the Wuhan National Laboratory for Optoelectronics, Huazhong University of Science and Technology, Wuhan 430074, P.R. China Contact e-mail: mgao@mail.hust.edu.cn

Manuscript submitted May 27, 2014.

Article published online February 18, 2015

metals. For example, Liu *et al.*^[21] obtained accepted Mg/Al joints, and Song *et al.*^[22] obtained good Mg/steel joints by Nd:YAG laser-tungsten inert gas (TIG) arc hybrid welding. Gao *et al.* obtained good Al/steel and Al/Ti joints by fiber laser-cold metal transfer (CMT) arc hybrid welding.^[17,19]

Although both laser-arc hybrid welding and Cu interlayer are interesting for joining dissimilar Ti alloy and SS, no prior work paid attention on this work. This article then aims to study laser-arc hybrid welding of dissimilar Ti6Al4V alloy and 316SS, and reveal the joint characterization and relevant mechanisms.

II. EXPERIMENTAL METHOD

Commercial Ti6Al4V alloy and AISI316L stainless steel (316SS) sheets with a thickness of 2 mm were used as the starting materials. Commercial Cu3Si wire (S211) with 1.0 mm in diameter was employed as the interlayer. Table I shows the mass chemical compositions of base metals and filler wire. Before welding, every sheet was cut and machined into pieces with the size of $100 \times 50 \times 2 \text{ mm}^3$ and a bevel of 10 deg on both sides along the direction of thickness. As shown in Figure 1, the samples were welded in butt configuration.

The equipment used includes a fiber laser (IPG YLR-6000, IPG Photonics Corporation, Oxford, MA), a CMT arc welder (TPS4000-CMT, Fronius International GmbH, Pettenbach, Austria), and a robot (KR60HA, KUKA Robot Group, Augsburg, Germany). The laser beam with a wavelength of 1070 nm and a beam parameter product of 6.9 mm mrad was transmitted by a 200 μm core-diameter fiber, collimated by a lens with 150 mm focal length, and then focused by a lens with 250 mm focal length to get a spot size of 0.33 mm. As shown in Figure 1, the angle of laser beam to vertical direction was 10° , and the angle of CMT torch to workpiece surface was 55° . The distance of laser beam to wire tip (D_{LA}) was 2 mm. The preliminary experiment showed that when laser beam deviated from seam center to Ti alloy, the joint fractured directly after welding because a high volume fraction of brittle Ti-Fe IMCs were formed. On the other hand, too large offset of laser beam from seam center to 316SS caused incomplete filled defect on Ti6Al4V sheet. Therefore, laser beam was set to irradiate on the edge of the bevel of 316SS sheet, as shown in Figure 1(a). The important parameters of the joints selected for discussion are listed in Table II.

Before welding, the sheet surfaces were cleared and degreased with acetone, and a flux of KF was pre-coated

on the groove surface of Ti6Al4V sheet. After welding, the specimens were polished and etched by a solution of (5 g) FeCl_3 , (5 mL) HCl, and (100 mL) ethanol. Microstructure and fracture morphologies were observed by scanning electron microscopy (SEM). Chemical compositions of specific areas were tested by energy dispersive spectrometry (EDS) technique. The IMCs were analyzed by scanning the fracture surfaces using X-ray diffraction technique (XRD). The rectangle cross-weld tensile samples were prepared as illustrated in Figure 2. The tensile test was carried out at room temperature, and the results were the average of three samples from the same weld.

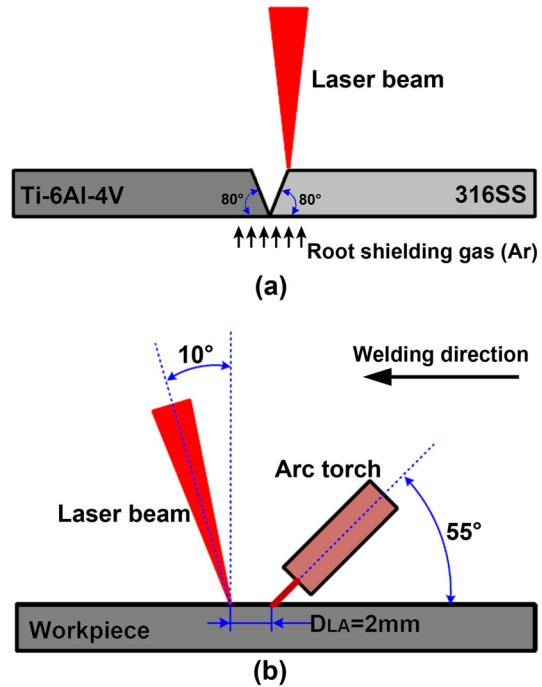


Fig. 1—Schematic diagram of set-up and joint groove, (a) frontal view, (b) side view.

Table II. Welding Parameters of Typical Joints

Specimen Number	#1	#2	#3
Laser power, P (kW)	1.5	2.0	3.0
Wire filling rate, r (m min^{-1})	6.8	6.8	9.0
Arc current, I (A)	110	110	130
Arc voltage, U (V)	10.5	10.5	12.5
Welding speed, v (m min^{-1})	1.5	3.0	5.0
Heat input, Q (J mm^{-1})	106	63	55

Table I. Mass Chemical Composition of Base Materials and Filler Wire

Materials	Chemical Composition (Wt. Pct)									
	Ni	Cr	Mn	Mo	Si	Al	V	Fe	Ti	Cu
316SS	12.6	17.83	1.80	2.35	0.78	—	—	bal.	—	—
Ti-6Al-4V	—	—	0.030	—	—	6.236	3.925	—	bal.	—
Cu3Si wire	—	—	0.5–1.5	—	2.8–4.0	—	—	—	—	bal.

III. RESULTS

A. Bead Morphology

As shown in Figure 3(a), the weld bead with uniform width is obtained at a high heat input of 106 J mm^{-1} and a slow welding speed of 1.5 m min^{-1} , but there is substantial melting of Ti6Al4V base metal. With the decrease of heat input, as shown in Figures 3(b) and (c), the beads become narrower, and concavities appear on the surface due to insufficient heat input and fast solidification rate. It is also found that the fusion zone (FZ) of joint #1 has single color throughout the cross section, while those of joint #2 and joint #3 show two kinds of color. Obviously, the microstructure of the FZ becomes more homogeneous with increasing heat input because the melted wire and base metals have more time to mix and react with each other.

B. Microstructure of Interfaces and FZ

Figures 4, 5, 6, and 7 provide microstructure details of each joint corresponding to the marked areas shown in Figure 3. Figure 8 is the XRD results of fracture surfaces. Tables III, IV, and V are the EDS results of the joints. Figures 9, 10, and 11 are ternary phase diagrams of Cu-Fe-Ti,^[23,24] Cu-Si-Ti,^[25] and Fe-Si-Ti,^[26,27] respectively. According to the phase diagrams and the

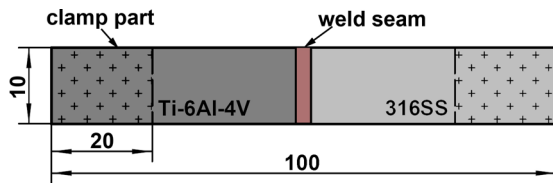


Fig. 2—Schematic diagram of tensile specimens.

test results, suggested phases of typical areas are listed in Tables III, IV, and V.

1. Microstructure of joint #1

In Figures 4(a), (b), and (f), the whole 316SS/FZ interface features a narrow bamboo-like 316SS rich in Si, Ti, and Cu, while the FZ nearby the interface consists of high volume fraction of bright α -Cu rich in Si and Fe. In Figures 4(c) and 4(d), the FZ/Ti6Al4V interface is characterized by a CuTi_2 layer, and it is thicker than the 316SS/FZ interface.

Figures 4(d), (e), (g), and (h) show that most of the FZ is composed of the dendrites. The density of the dendrites nearby the CuTi_2 layer is higher than that in the center. The compositions of the areas T17, T19, and T110 suggest that the dark arm of the dendrites is the $\text{Fe}_{67-x}\text{Si}_x\text{Ti}_{33}$, while the bright phase between the arms is the α -Cu. In Figure 3(g) (area T18), some needle compounds of $\text{Cu}_{67-x}\text{Fe}_x\text{Ti}_{33}$ rich in Ti appear between the dendrite arms close to the FZ/Ti6Al4V interface. Figure 5 reveals the penetration of Cu element along the grain boundaries into the 316SS base metal.

2. Microstructure of joint #2

Figure 6(a) shows that the upper part of 316SS/FZ interface is a 316SS rich in Si and Cu, while the FZ nearby this interface is composed of massive α -Cu but contains a small volume fraction of $\text{Fe}_{67-x}\text{Si}_x\text{Ti}_{33}$ particles. Figure 6(b) shows that the lower part of 316SS/FZ interface consists of a wider mixture of $\text{Fe}_{67-x}\text{Si}_x\text{Ti}_{33}$ and 316SS, while the FZ nearby the interface is composed of compact dendrites of $\text{Fe}_{67-x}\text{Si}_x\text{Ti}_{33}$.

Figure 6(c) indicates that the upper part of FZ/Ti6Al4V interface is a CuTi layer with dark-light stripes. Figure 6(h) shows that some quadratic Ti_5Si_3 sticks occur in the α -Cu matrix nearby the CuTi layer. The EDS analysis shows that this area lacks Fe, which suggests that the movement of Fe atoms from the

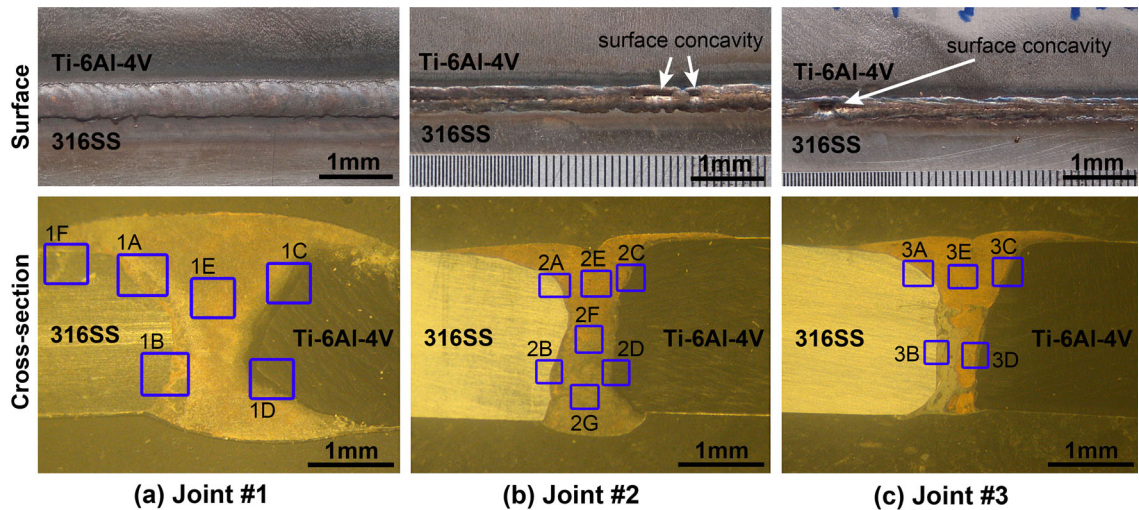


Fig. 3—Surface and cross-section morphologies, (a) joint #1, (b) joint #2, (c) joint #3.

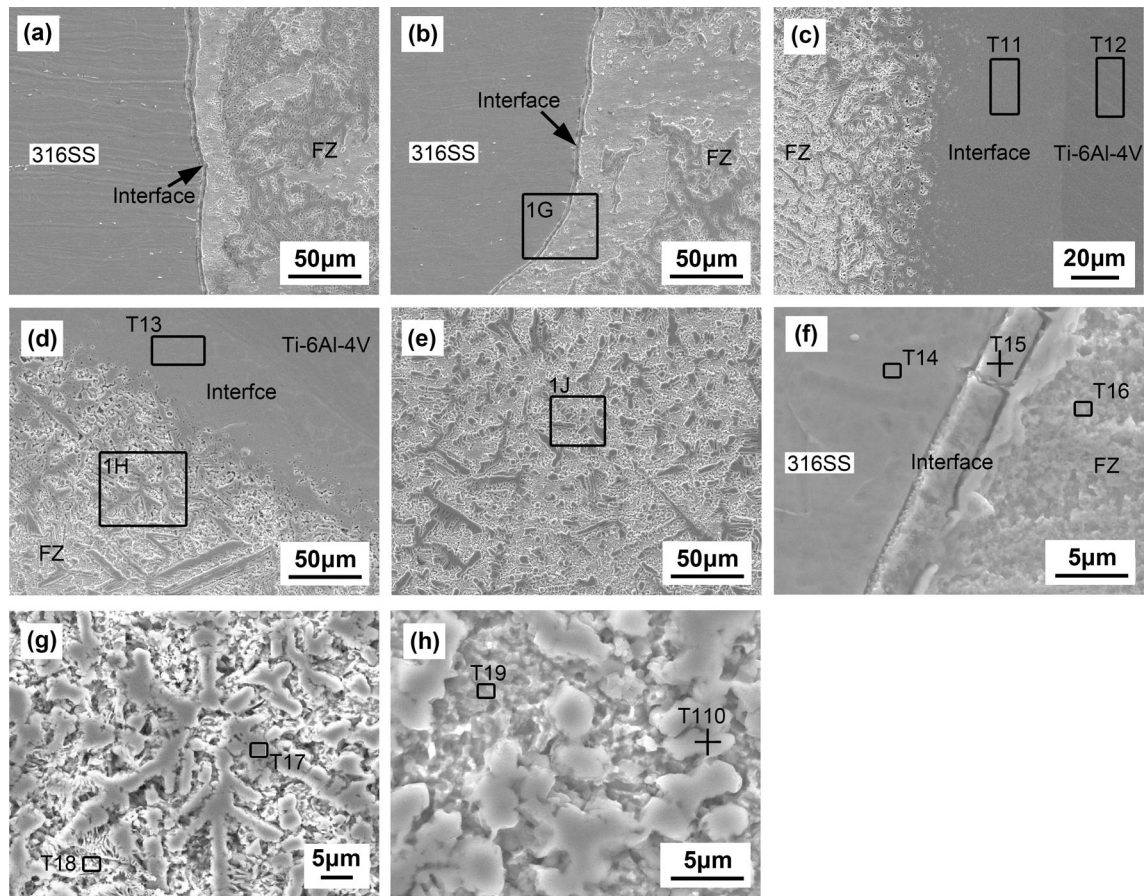


Fig. 4—Microstructure of joint #1, (a) to (e) refer to the areas in Fig. 3(a): (a) 1A, upper part of 316SS/FZ interface, (b) 1B, lower part of 316SS/FZ interface, (c) 1C, upper part of FZ/Ti6Al4V interface, (d) 1D, lower part of FZ/Ti6Al4V interface, and (e) 1E, middle FZ; (f) to (h) refer to the areas in this figure: (f) 1G, (g) 1H, (h) 1J.

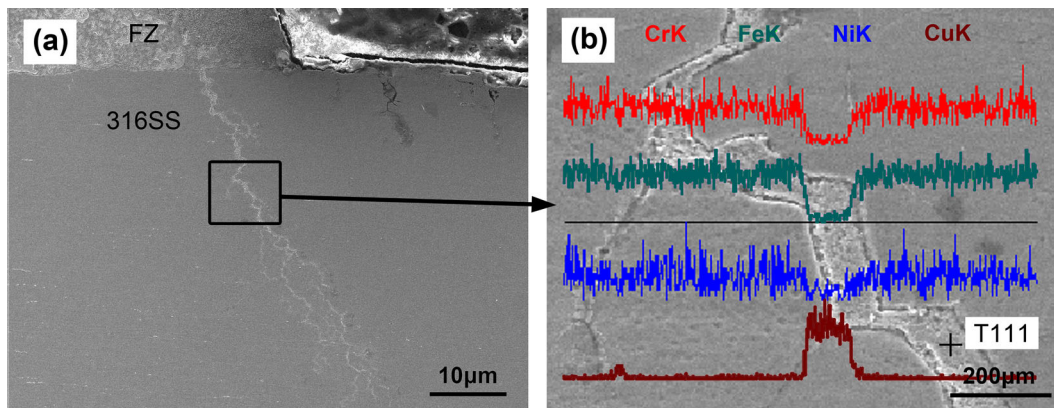


Fig. 5—Intergranular penetration at 316SS of joint #1, (a) macro image corresponding to the area 1F in Fig. 3(a), (b) enlarged image with EDS line scanning.

316SS/FZ interface to this area is suppressed. Figure 6(d) shows that the lower part of FZ/Ti6Al4V interface is a CuTi_2 layer rich in Fe.

In Figures 6(e) and (i), it can be seen that the upper FZ consists of a large scale of α -Cu and a small volume fraction of fish bone or needle $\text{Fe}_{67-x}\text{Si}_x\text{Ti}_{33}$. Figure 6(f) shows that the middle FZ is a mixture of planar α -Cu and worm-like $\text{Fe}_{67-x}\text{Si}_x\text{Ti}_{33}$. Figure 6(g) shows that the

lower FZ consists of a large volume fraction of worm-like $\text{Fe}_{67-x}\text{Si}_x\text{Ti}_{33}$ and a few α -Cu between the ‘worms.’ In Table V, the chemical compositions of the areas T211, T213, and T217 suggest that the Cu content in the $\text{Fe}_{67-x}\text{Si}_x\text{Ti}_{33}$ of these areas decreases from the upper zone to the lower zone.

The above results suggest that the melted Cu wire prefers to stay in the upper pool under this parameter

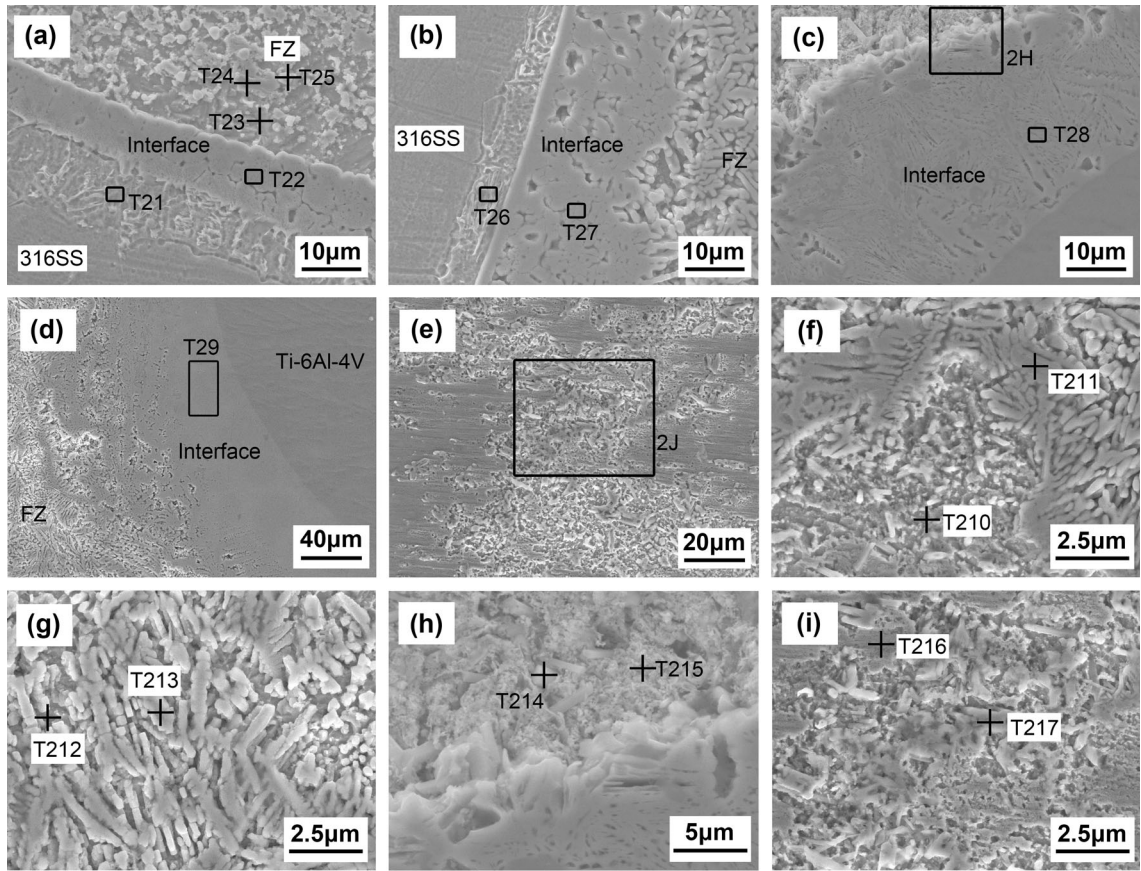


Fig. 6—Microstructure of joint #2. (a) to (g) refer to the areas in Fig. 3b: (a) 2A, upper part of 316SS/FZ interface, (b) 2B, lower part of 316SS/FZ interface, (c) 2C, upper part of FZ/Ti6Al4V interface, (d) 2D, lower part of FZ/Ti6Al4V interface, (e) 2E, upper FZ, (f) 2F, middle FZ, (g) 2G, lower FZ; (h) and (i) refer to areas in this figure: (h) 2H, (i) 2J.

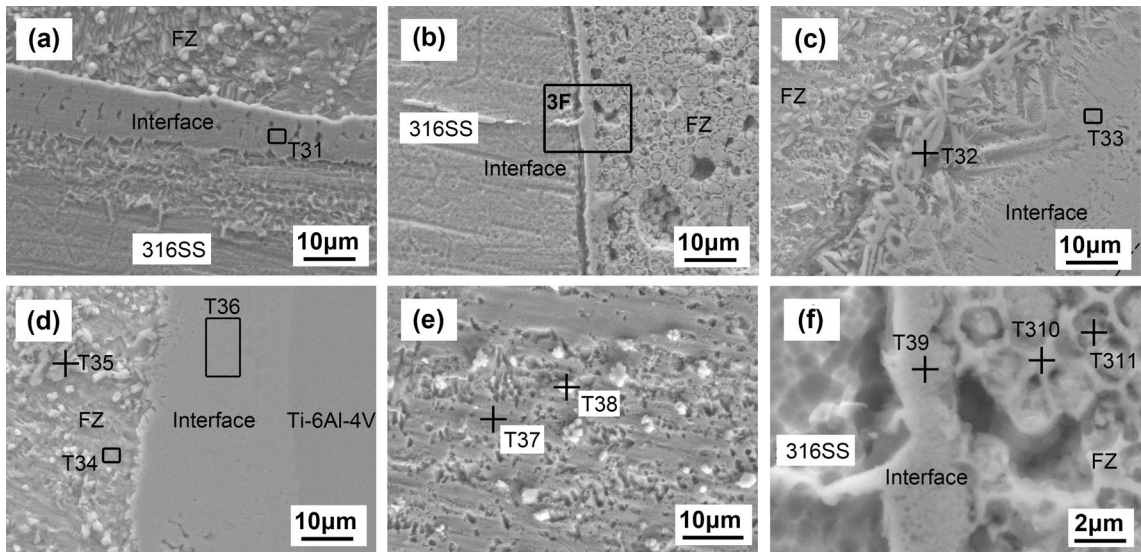


Fig. 7—Microstructure of joint #3, (a) to (e) refer to the areas in Fig. 3(c): (a) 3A, upper part of 316SS/FZ interface, (b) 3B, lower part of 316SS/FZ interface, (c) 3C, upper part of FZ/Ti6Al4V interface, (d) 3D, lower part of FZ/Ti6Al4V interface, (e) 3E, upper FZ; (f) refers to area 3F in this figure.

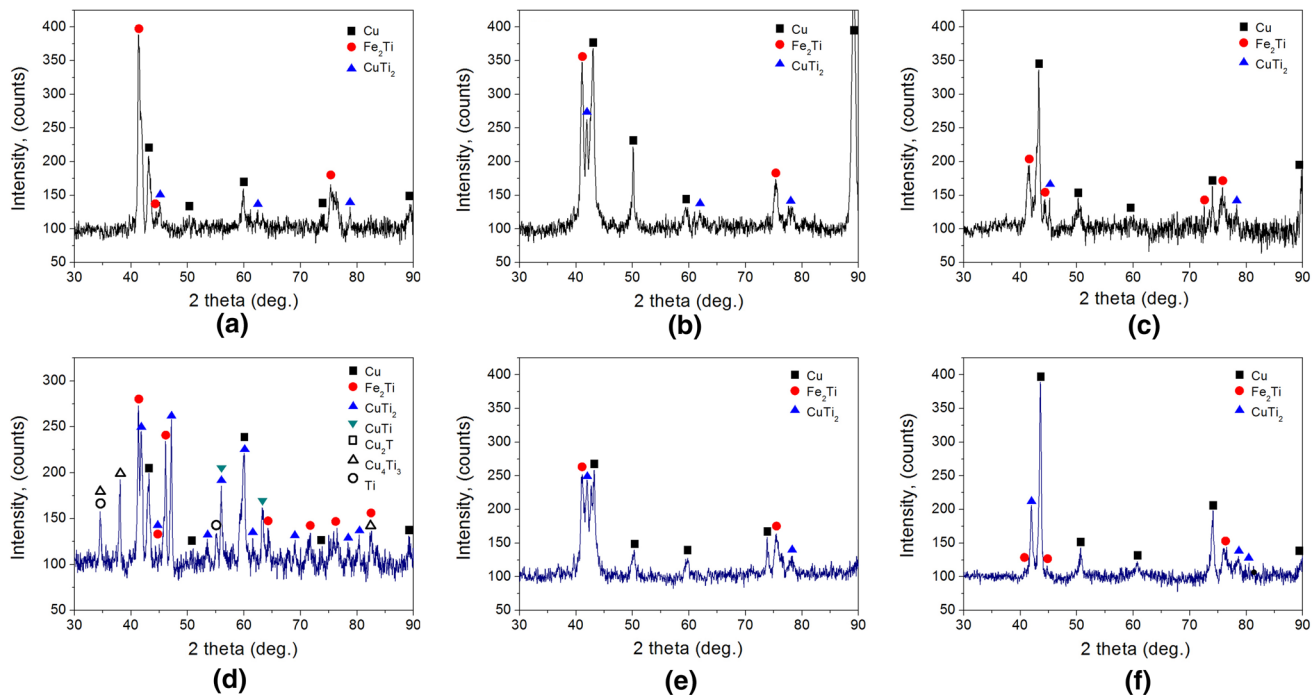


Fig. 8—XRD analysis results on the fracture surfaces, (a) 316SS side of joint #1, (b) 316SS side of joint #2, (c) 316SS side of joint #3, (d) Ti6Al4V side of joint #1, (e) Ti6Al4V side of joint #2, (f) Ti6Al4V side of joint #3.

Table III. Molar Chemical Compositions of Joint #1

Point	Chemical Compositions (At. Pct)	Suggested Phase
T11	25.57Cu-8.62Fe-47.72Ti-3.64Si-2.25Cr-2Ni-7.58Al-2.62V	CuTi ₂
T12	84.03Ti-12.85Al-3.12V	Ti-6Al-4V
T13	23.63Cu-7.29Fe-52.57Ti-2.61Si-1.45Cr-1.25Ni-8.87Al-2.35V	CuTi ₂
T14	68.65Fe-1.88Si-18.17Cr-9.77Ni-1.53Mo	316SS rich in Si
T15	3.59Cu-60.86Fe-3.46Ti-4.12Si-18.64Cr-6.3Ni-0.60V-1.39Mo-1.00Mn	316SS rich in Si, Ti, and Cu
T16	90.54Cu-3.49Fe-5.96Si	α -Cu rich in Fe and Si
T17	7.26Cu-32.19Fe-29.37Ti-18.21Si-8.00Cr-2.38Ni-1.35V-1.27Mo	Fe _{67-x} Si _x Ti ₃₃
T18	42.43Cu-9.86Fe-24.41Ti-1.85Si-2.30Cr-2.29Ni-1.28Al-0.42V-15.57O	Cu _{67-x} Fe _x Ti ₃₃
T19	90.46Cu-5.07Fe-2.04Ti-2.43Si	α -Cu rich in Fe, Ti, and Si
T110	5.06Cu-35.59Fe-27.52Ti-18.61Si-7.78Cr-2.57Ni-1.46V-1.41Mo	Fe _{67-x} Si _x Ti ₃₃

Table IV. Molar Chemical Compositions of Joint #2

Point	Chemical Compositions (At. Pct)	Suggested Phases
T21	67.67Fe-1.43Si-19.39Cr-10.05Ni-1.46Mo	316SS rich in Si
T22	6.27Cu-59.10Fe-9.8Si-16.41Cr-6.32Ni-2.09Mo	316SS rich in Si, Cu
T23	87.48Cu-7.55Si-4.97Fe	α -Cu rich in Si and Fe
T24	92.56Cu-4.61Si-2.83Fe	α -Cu rich in Si and Fe
T25	8.28Cu-44.75Fe-26.14Si-12.20Cr-3.67Ni-0.49Mo-3.0Ti-0.21V-1.27Mn	Fe _{67-x} Si _x Ti ₃₃
T26	65.38Fe-2.47Si-17.87Cr-10.48Ni-1.98Mo-1.82Mn	316SS rich in Si
T27	5.33Cu-46.74Fe-19.97Ti-5.7Si-12.82Cr-5.54Ni-1.19Al-0.93V-1.18Mo-0.6Mn	Fe _{67-x} Si _x Ti ₃₃ + 316SS
T28	38.38Cu-46.93Ti-7.93Si-5Al-1.75V	CuTi
T29	24.77Cu-8.39Fe-50.31Ti-2.45Si-1.85Cr-8.42Al-2.24V	CuTi ₂
T210	100Cu	α -Cu
T211	16.96Cu-32.31Fe-22.72Ti-14.36Si-7.93Cr-3.09Ni-1.45V-1.19Mo	Fe _{67-x} Si _x Ti ₃₃
T212	83.15Cu-6.05Fe-5.32Ti-2.01Cr-1.46Ni-0.55V-1.44Mn	α -Cu
T213	8.56Cu-36.70Fe-25.17Ti-14.36Si-9.43Cr-3.97Ni-0.82V-0.99Mo	Fe _{67-x} Si _x Ti ₃₃
T214	11.65Cu-50.46Ti-35.65Si-2.25V	Ti ₅ Si ₃
T215	90.13Cu-4.73Ti-4.53Si-0.61V	α -Cu rich in Ti and Si
T216	96.43Cu-3.57Si	α -Cu
T217	20.06Cu-30.86Fe-20.30Ti-23.41Si-1.93Cr-1.99Ni-0.57V-0.89Mn	Fe _{67-x} Si _x Ti ₃₃

Table V. Molar Chemical Compositions of Joint #3

Point	Chemical Compositions (At. Pct)	Suggested Phases
T31	5.36Cu-60.77Fe-7.03Si-17.35Cr-7.29Ni-2.2Mo	316SS rich in Cu and Si
T32	4.09Cu-1.06Fe-52.40Ti-37.00Si-1.18Cr-3.94V-00.32Mn	Ti ₅ Si ₃
T33	47.06Cu-43.04Ti-4.78Si-3.01Al-2.11V	CuTi
T34	90.96Cu-3.09Fe-5.95Si	α-Cu rich in Fe and Si
T35	10.2Cu-22.73Fe-26.40Ti-29.33Si-4.91Cr-2.9Ni-2.3V-0.58Mo-0.65Mn	Fe _{67-x} Si _x Ti ₃₃
T36	27.4Cu-9.61Fe-47.55Ti-3.18Si-2.26Cr-1.27Ni-7.02Al-1.71V	CuTi ₂
T37	93.26Cu-2.52Fe-4.22Si	α-Cu rich in Fe and Si
T38	15.06Cu-26.01Fe-23.81Ti-25.91Si-5.39Cr-1.56Ni-0.69V-1.11Mo-0.44Mn	Fe _{67-x} Si _x Ti ₃₃
T39	7.13Cu-54.03Fe-6.87Ti-6.8Si-14.68Cr-6.95Ni-2.5Mo-1.04Mn	316SS rich in Si, Ti, and Cu
T310	8.26Cu-50.78Fe-10.67Ti-6.53Si-13.28Cr-7.48Ni-0.48Al-1.73Mo-0.79Mn	316SS rich in Si, Ti, and Cu
T311	6.19Cu-58.39Fe-4.85Ti-4.36Si-15.75Cr-6.77Ni-1.53Al-1.23Mo-0.95Mn	316SS rich in Si, Ti, and Cu

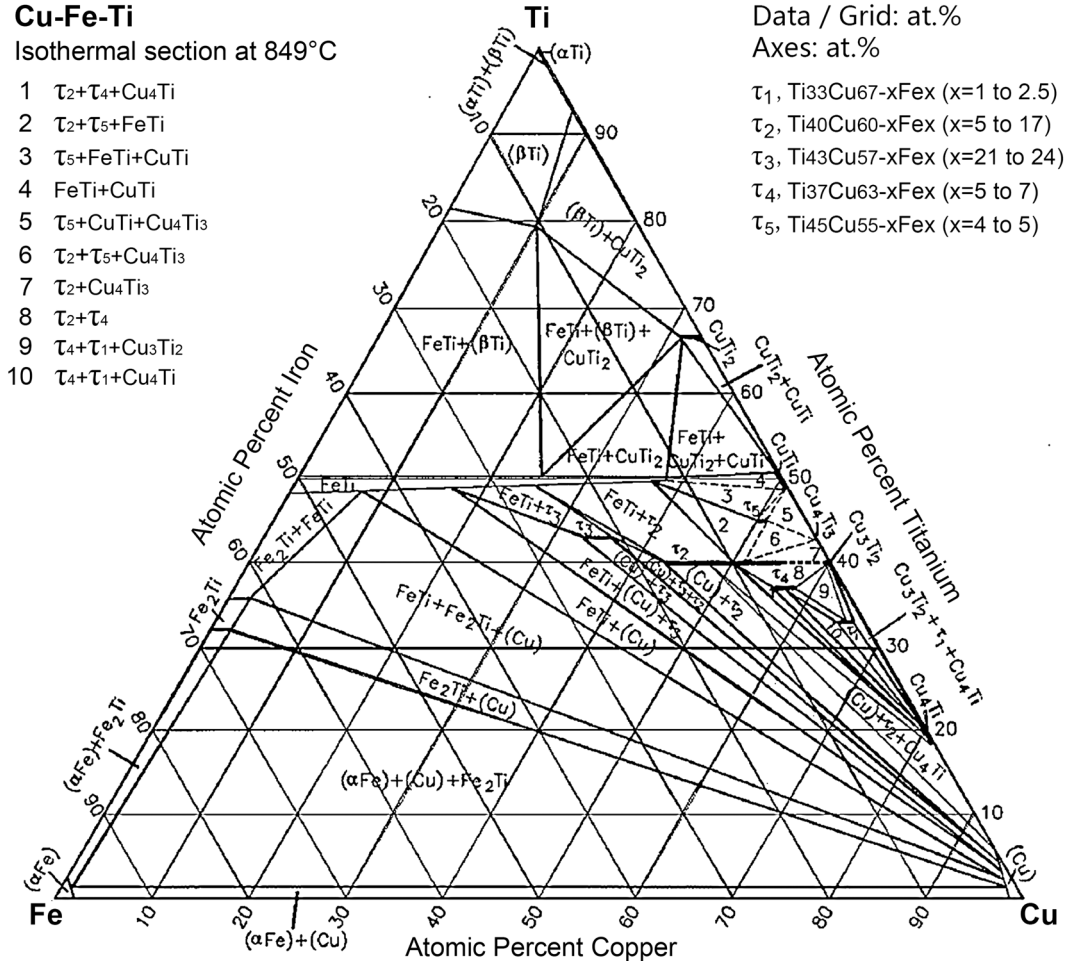


Fig. 9—Ternary phase diagram of Cu-Fe-Ti isothermal section at 1122 K (849 °C).^[23,24] For clarity, thin two-phase fields around tie-triangles are omitted.

combination. It hampers the direct reaction between Fe and Ti in the upper FZ and consequently leads to the microstructure difference from the top to the bottom within the joint.

3. Microstructure of joint #3

Figure 7(a) shows that the microstructure of the upper part of 316SS/FZ interface of joint #3 is similar

with that of joint #2, which is the 316SS rich in Si and Cu. Figure 7(e) shows that the upper FZ is composed of a large scale of α-Cu and a few round Fe_{67-x}Si_xTi₃₃ particles. In Figure 7(b), the lower part of 316SS/FZ interface is also the 316 SS, but the width of the interface is smaller than that of upper part. It can be seen that some 316SS cells appear in the FZ nearby the lower part of 316SS/FZ interface. The cell frame has higher content

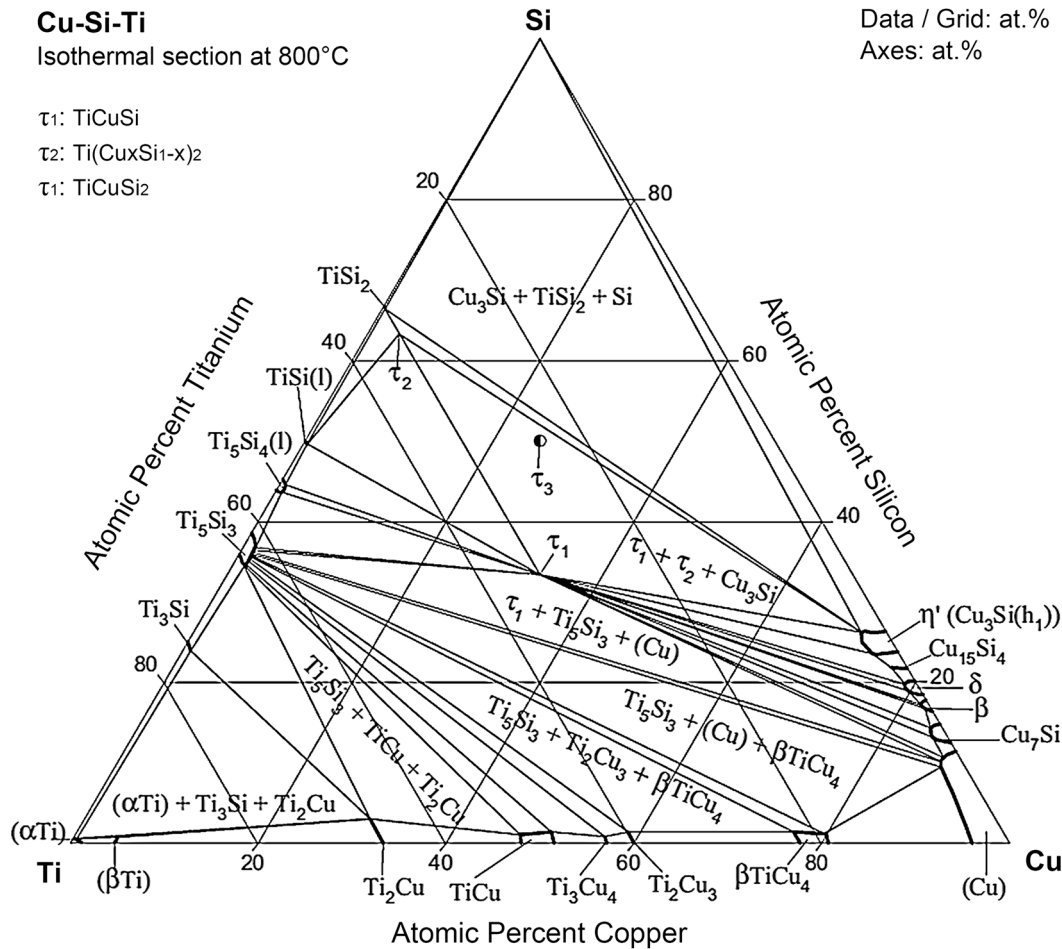


Fig. 10—Ternary phase diagram of Cu-Si-Ti Isothermal section at 1073 K (800 °C)^[25].

of Cu, Ti, and Si, and lower content of Fe and Cr than the inner. It suggests that the Cu is prevented from entering to the lower part of FZ/316SS interface when the heat input is small.

Figure 7(c) shows that the upper part of FZ/Ti6Al4V interface is a CuTi layer, while the FZ nearby this interface is characterized by some Ti₅Si₃ sticks in α -Cu matrix. Figure 7(d) shows that the lower part of FZ/Ti6Al4V interface is a CuTi₂ layer, while the FZ nearby this interface is the α -Cu with some Fe_{67-x}Si_xTi₃₃ dendrites or particles.

C. Microhardness

Figure 12 gives the microhardness distribution across weld transverse surface. Four findings can be seen. Firstly, the CuTi₂ layer at the FZ/Ti6Al4V interface is the hardest area for each joint with the hardness higher than 400 HV0.1. Secondly, the areas whose microhardness is lower than that of 316SS base metal are characterized by a large scale of α -Cu, as shown in Figures 12(b) and (c). Thirdly, the microhardness increases from the 316SS base metal to the FZ/Ti6Al4V interface, except for above-mentioned areas that are softer than the 316SS base metal. Finally, the micro-

hardness variations within one joint are well in accordance with the microstructure described above. For the joint #1 with more homogeneous microstructures, the microhardness of the upper zone and the lower zone has similar variation.

D. Tensile Strength and Fractograph

As shown in Figure 13, the tensile strength of cross weld decreases with the decrease of heat input. The joint #1 with the most homogeneous microstructure has the highest tensile strength of 212 MPa, which is about three times that of joint #3. In the previous studies,^[10,11] the tensile strengths of the Ti/SS joint welded by electron beam welding with Cu interlayer and laser welding with Mg interlayer were up to 224 and 221 MPa, respectively. This indicates that the tensile strengths of the joints made in this study are of the same order as those reported made in earlier studies. However, compared with electron beam welding, laser-arc hybrid welding does not need vacuum environment. Compared with Mg interlayer, the Cu interlayer used in this study can improve high-temperature performance and corrosion resistance of the joints. Hence, laser hybrid welding with Cu interlayer is more suitable for industrial applications.

Fe-Si-Ti

Isothermal section at 900 °C

- τ_1 : FeSi₅Ti
- τ_2 : FeSiTi
- τ_3 : Fe₄Si₃Ti

Data / Grid: at. %

Axes: at. %

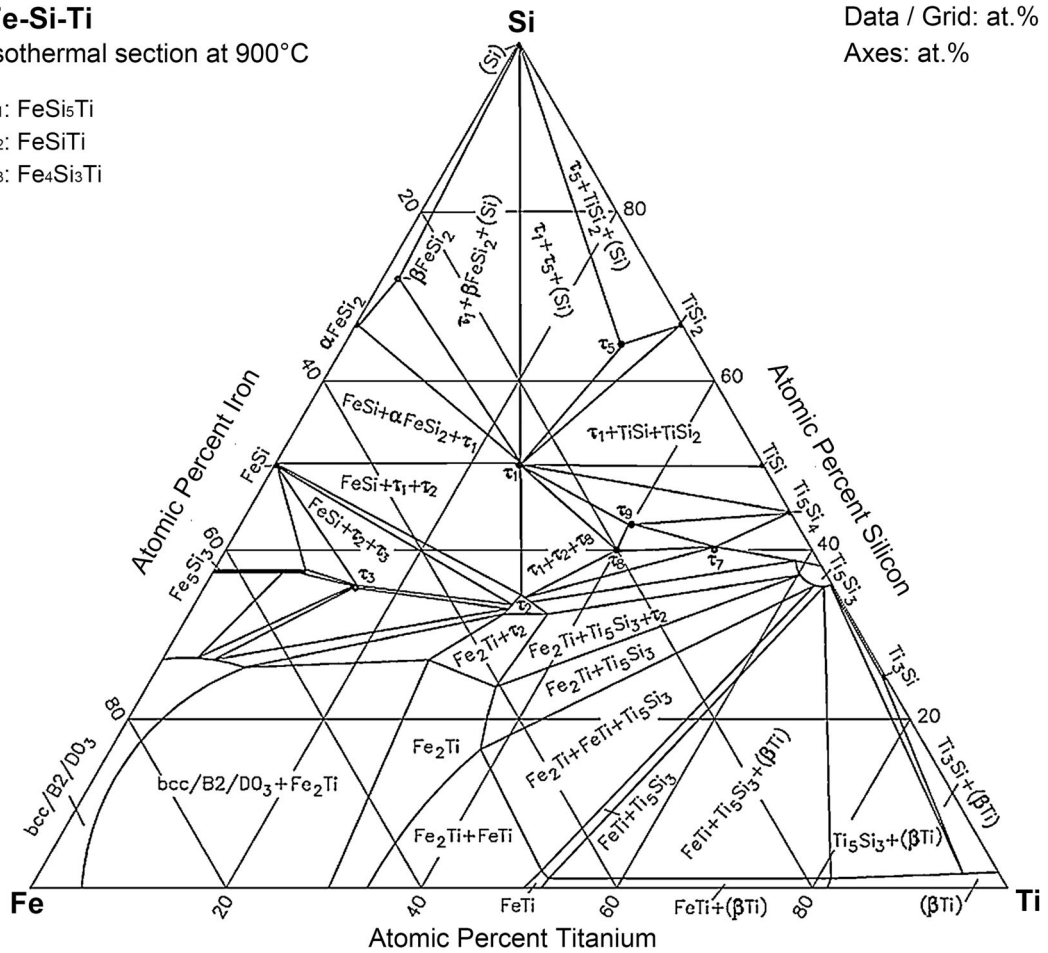


Fig. 11—Ternary phase diagram of Fe-Si-Ti tentative isothermal section at 1173 K (900 °C),^[26,27] narrow two-phase regions are omitted here.

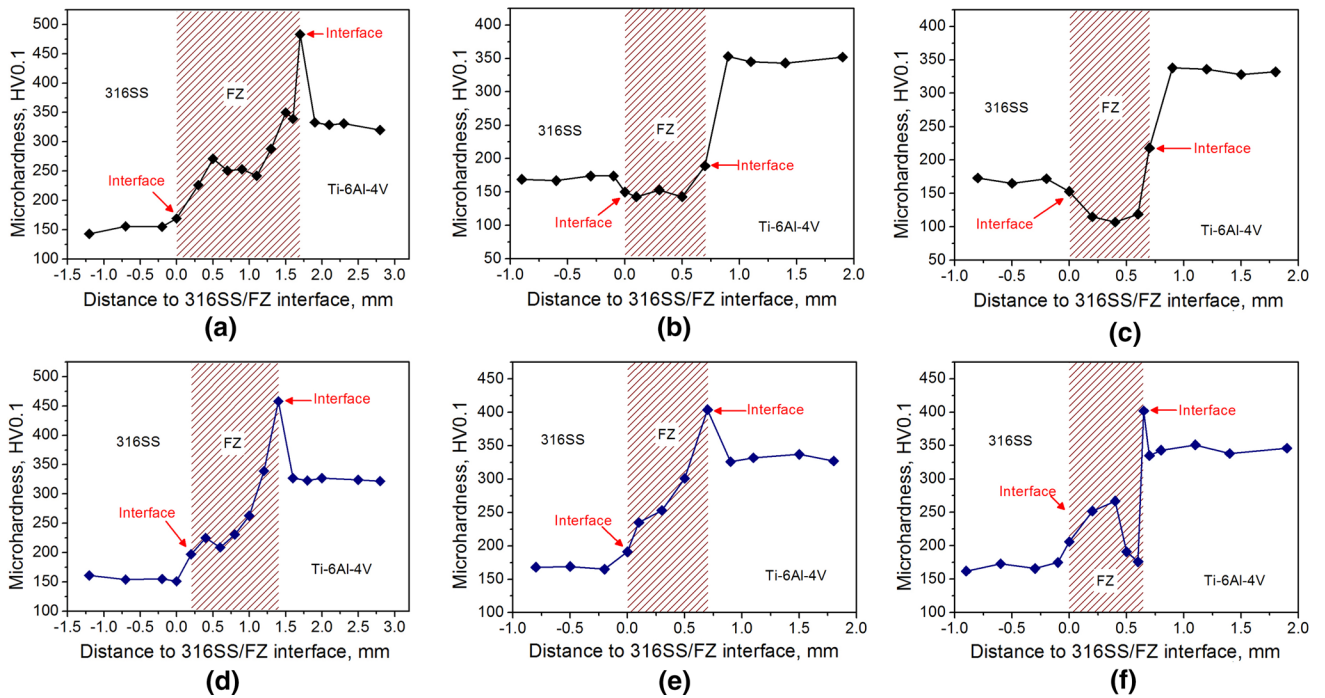


Fig. 12—Microhardness across weld transverse surface, (a) upper zone of joint #1, (b) upper zone of joint #2, (c) upper zone of joint #3, (d) lower zone of joint #1, (e) lower zone of joint #2, (f) lower zone of joint #3.

All the joints fracture at the FZ/Ti6Al4V interface during tensile tests. For brief, the fracture side including the Ti6Al4V base metal is named as Ti6Al4V side, while that including both the 316SS base metal and the FZ is named as 316SS side. Figures 14, 15, and 16 show the fractographs of tensile samples. The fracture surfaces of both the 316SS side and the Ti6Al4V side are characterized by river pattern revealing brittle cleavage fracture mode. Table VI shows that the river pattern is composed of CuTi_2 . Then, the CuTi_2 layer at the FZ/Ti6Al4V interface is the weakest zone within the joint.

As shown in Figure 15, for the joint #2, some cavities characterized by round-tip dendrites are found at the 316SS side, while some KAlF_4 needles appear at the Ti6Al4V side. The KAlF_4 comes from the reaction between pre-coated flux and Al element contained in the Ti6Al4V base metal. In Figure 16, obvious secondary cracks and a large scale of particles appear on the fracture surfaces of joint #3. According to the EDS results, the particles at 316SS side are identified as oxide inclusions, while those at Ti6Al4V side are identified as oxidized α -Cu. The oxides denote that some areas at the FZ/Ti6Al4V interface of joint #3 are not fused during welding because of low heat input. These defects

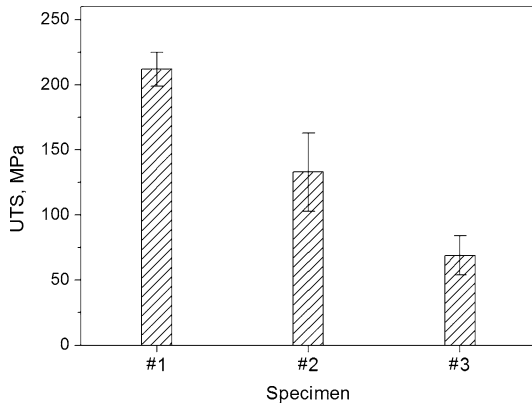


Fig. 13—Tensile strength of typical joints.

including the incomplete fusion and the cavities at the interface are the main reasons that decrease the tensile strength.

IV. DISCUSSION

A. Microstructure Difference

During hybrid welding, both the temperature and chemical compositions in the molten pool are influenced by the melt flow that is closely related to laser-arc synergic effect,^[28] and the reaction time is related to the solidification rate that depends on the heat input and the welding speed. In this study, the main elements in the molten pool are Cu, Si, Fe, and Ti, while the other minor elements are Cr, Ni, Al, and V. The binary phase diagrams show that the minor elements mentioned above cannot react with these main elements of Cu, Si, Fe, and Ti. Moreover, Cu and Si prefer to appear together because both of them come from the filler wire. Therefore, possible systems in the molten pool are Cu-Si-Fe ternary system, Cu-Si-Ti ternary system, and Cu-Si-Fe-Ti quaternary system. By this viewpoint, the formation of the microstructure difference within one joint and between the joints is illustrated in Figure 17 and described as follows.

1. In Figure 17(a), a volume fraction of melted 316SS, Ti6Al4V, and filler wire (Cu_3Si) in the molten pool are represented in terms of the incident position of laser beam and the groove gap. The groove gap is filled by the melted filler wire. The volume fraction of melted 316SS is far larger than that of the Ti6Al4V because the laser beam directly irradiates on the 316SS. For the molten pool during hybrid welding, a downward flow from top to bottom is formed by arc pressure and surface tension along laser keyhole,^[29] and an upward flow from bottom to top is formed by the buoyancy due to the density difference between heavier filler wire and lighter base metals.

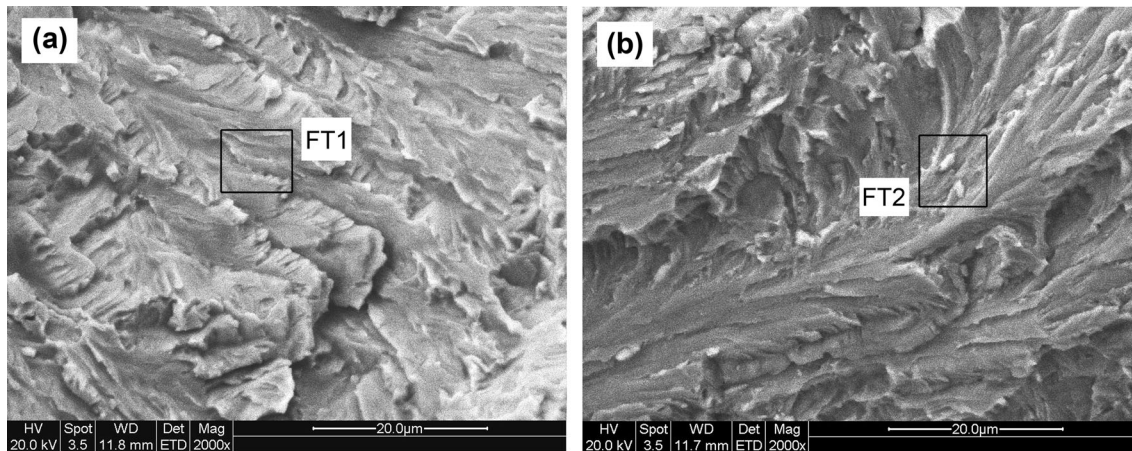


Fig. 14—Fractograph of joint #1, (a) 316SS side, (b) Ti6Al4V side.

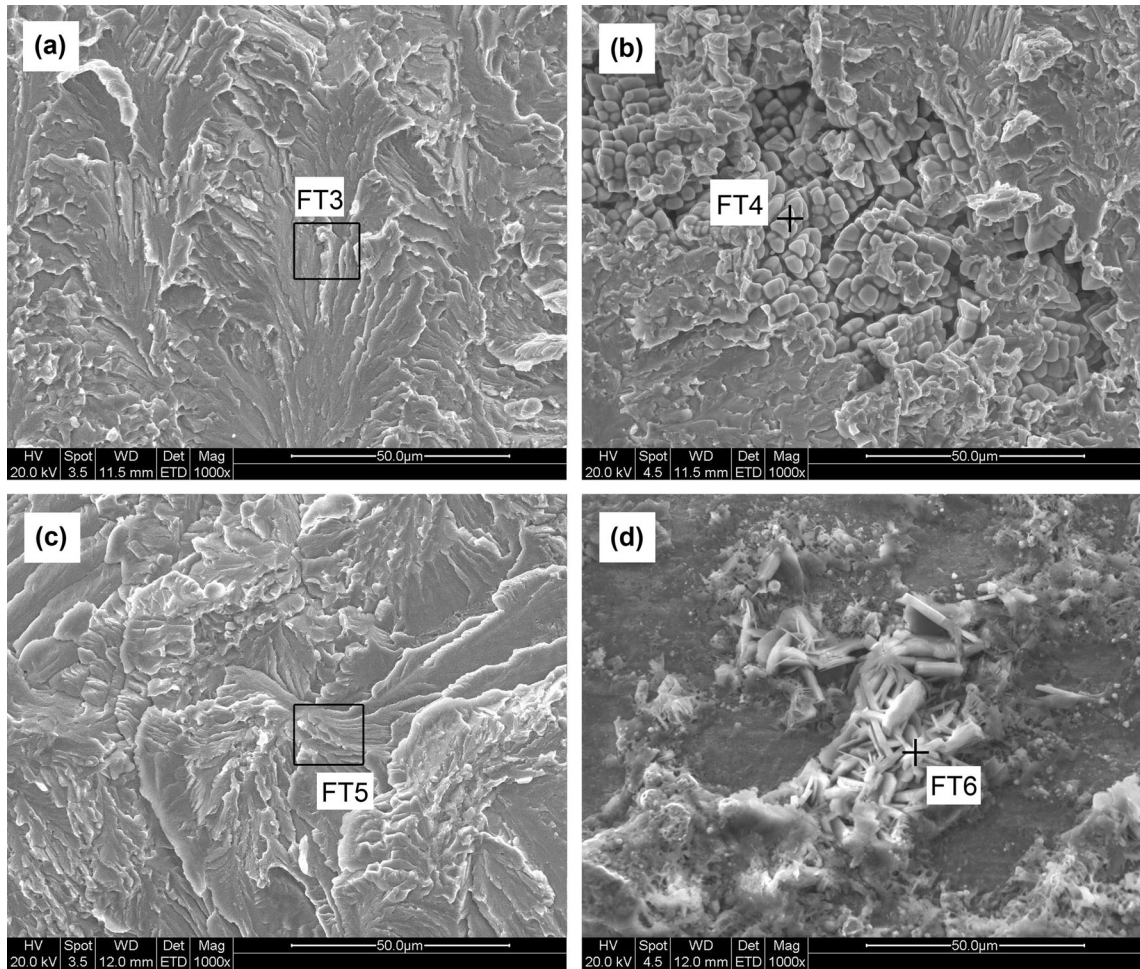


Fig. 15—Fractograph of joint #2, (a) river pattern at 316SS side, (b) solidified cavity at 316SS side, (c) river pattern at Ti6Al4V side, (d) inclusions at Ti6Al4V side.

2. The liquid Cu3Si mixes with the melted 316SS and Ti6Al4V *via* the melt flow. It shapes a distributing characterization as shown in Figure 17(b). The joint #3 shown in Figure 3(c) just solidifies at this stage. The narrow bead denotes that a small volume fraction of 316SS and Ti6Al4V base metals are melted due to low heat input. The molten pool is then composed of liquid Cu3Si but a small volume fraction of Fe and Ti atoms. The low-right area close to the 316SS base metal has no time to mix with the filler wire and prefers to keep the 316SS despite that a few Cu, Si, and Ti atoms diffuse in it. The fast solidification rate also hinders the Ti atoms from transferring to the 316SS/FZ interface and hinders the Fe atoms from moving to the FZ/Ti6Al4V interface. As a result, the top-left area adjacent to the 316SS/FZ interface is a Cu-Fe-Si ternary system, while the area close to the

FZ/Ti6Al4V interface is a Cu-Si-Ti ternary system. Another notable phenomenon is that, for the joint solidified at this stage, the lower heat input used would cause some poor fused area at the FZ/Ti6Al4V interface because of the fast solidification rate, which is proved by the oxides on the fracture surfaces shown in Figure 16.

3. With the increase of the heat input, the solidification rate decreases to proceed the mixing of molten pool. The low-left liquid 316SS tends to mix with the molten metal nearby. Because Cu element is heavier than Fe element, the upward tendency of liquid 316SS at the lower part is restrained by upper liquid Cu, and the mixture in the lower part occurs first. It shapes a distributing characterization as shown in Figure 17(c). The joint #2 in Figure 3(b) solidifies at this stage. Here, the upper FZ is composed of a large volume fraction of liquid

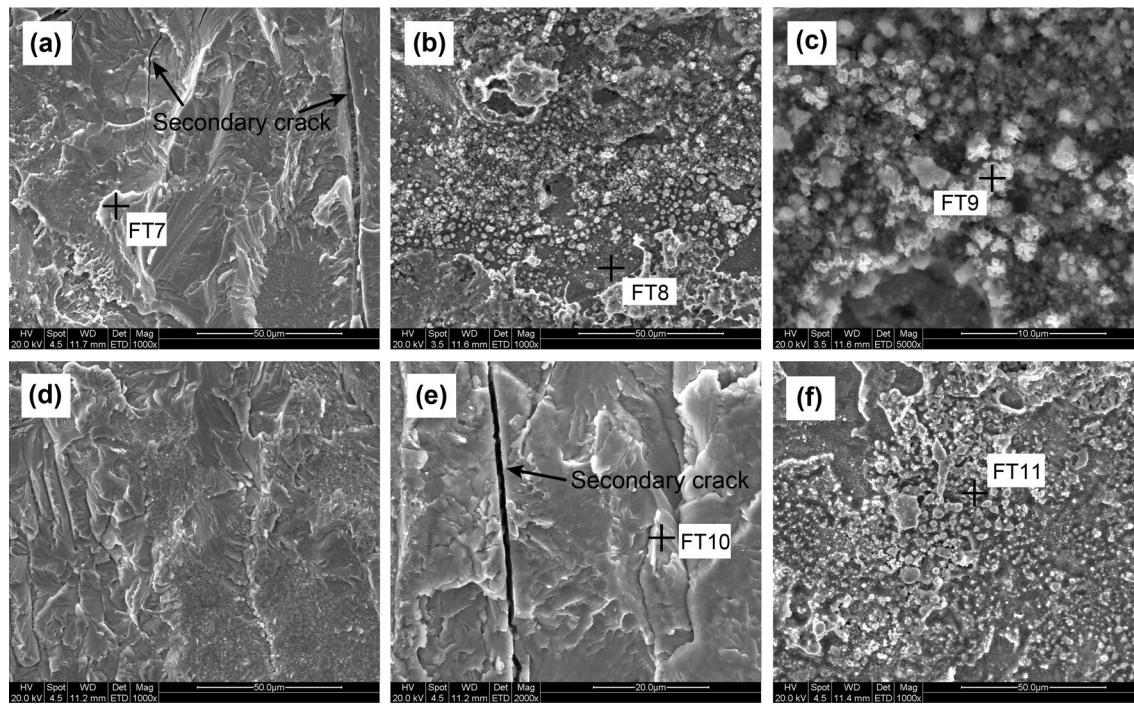


Fig. 16—Fractograph of joint #3, (a) typical fractograph of 316SS side, (b) oxidized inclusions at 316SS side, (c) amplified image of inclusions at 316SS side, (d) typical fractograph of Ti6Al4V side, (e) secondary cracks at Ti6Al4V side, (f) oxidized α -Cu particles at Ti6Al4V side.

Table VI. Molar Chemical Compositions of Fracture Surfaces

Point	Chemical Compositions (At. Pct)	Suggested Phase
FT1	23.31Cu-12.43Fe-45.51Ti-4.25Si-4.13Cr-2.23Ni-7.16Al-2.2V-0.79Mn	CuTi ₂
FT2	25.08Cu-9.09Fe-50.06Ti-3.03Si-1.44Cr-1.64Ni-8.75-1.24V-0.68Mn	CuTi ₂
FT3	19.81Cu-15.29Fe-40.37Ti-9.5Si-5.41Cr-2Ni-4.12Al-2.31V-1.21Mn	CuTi ₂
FT4	35.91Cu-2.44Fe-46.37Ti-1.44Si-11.68Al-2.15V	CuTi ₂
FT5	23.27Cu-10.71Fe-49.98Ti-2.41Si-2.06Cr-1.2Ni-7.59Al-2.25V-0.53Mn	CuTi ₂
FT6	2.24Fe-1.75Ti-11.14Al-0.65Mn-13.84O-50.02F-11.24K	KAlF ₄
FT7	13.91Cu-16.52Fe-53.61Ti-3.76Cr-3.19Ni-7.1Al-1.44V-0.47Mn	CuTi ₂
FT8	7.61Cu-28.93Fe-10.61Ti-5.77Si-8.26Cr-1.18Al-0.512V-0.65Mo-31.65O-0.92K	Fe ₂ Ti + CuO
FT9	25.56Cu-15.81Fe-4.64Ti-6Cr-1.7Ni-1.79Al-1.21Mn-41.76O-1.53K	CuO + Fe ₂ O ₃
FT10	18.55Cu-12.62Fe-58.61Ti-1.73Cr-3.19Al-2.63V	CuTi ₂
FT11	60.52Cu-8.76Fe-4.18Ti-2.33Ni-2.47Al-0.32V-7.45Mn-13.97O	oxidized α -Cu

filler wire (Cu₃Si) but a few Fe and Ti atoms, while the lower FZ is a Cu-Fe-Si-Ti quaternary system. Accordingly, the upper part of 316SS/FZ interface is a Cu-Fe-Si ternary system. The upper part of FZ/Ti6Al4V interface is a Cu-Si-Ti ternary system. The lower parts of both 316SS/FZ and FZ/Ti6Al4V interfaces are Cu-Fe-Si-Ti quaternary system.

- As the heat input is increased to be sufficient, the liquid pool has enough time to mix thoroughly to obtain a homogeneous joint as shown in Figure 17(d). Here, the whole molten pool is a Cu-Fe-Si-Ti quaternary system. Figure 3(a) shows that the joint #1 with the highest heat input solidifies at this stage.

B. Thermodynamic Mechanism of Microstructure Formation

The thermodynamic behavior plays a big role in the IMCs formation during welding. Because Cu does not react with Fe and Si, possible binary systems in the molten pool of this study are Fe-Ti, Cu-Ti, Fe-Si, and Ti-Si systems. According to the Miedema model established by Miedema^[30] and improved by Davies *et al.*^[31], standard molar enthalpy of formation (ΔH) of possible binary systems is calculated and illustrated in Figure 18.

According to the chemical composition of Cu₃Si filler wire, the mass content of Si element in the molten pool of this study is no more than 4 pct. Moreover, the Si

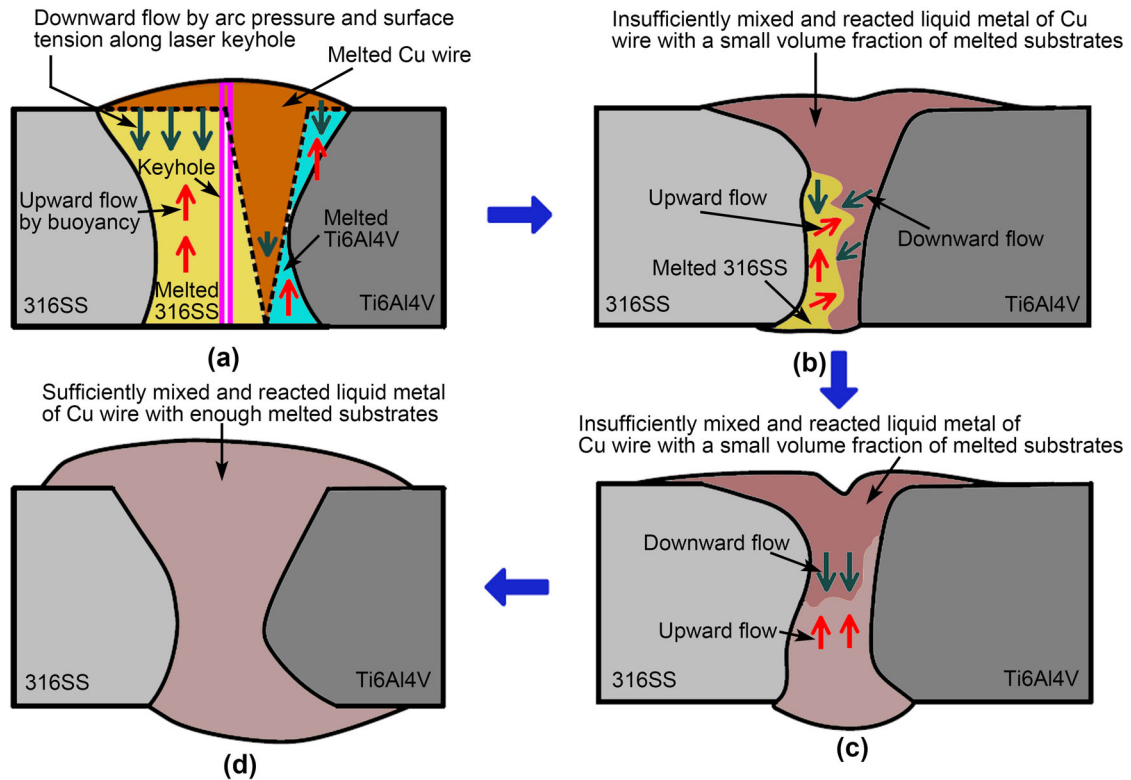


Fig. 17—Bead formation mechanism, (a) the distribution of melted materials and possible flows in molten pool, (b) to (d) refer bead shape and materials distribution under different parameters: (b) insufficient heat input and fast welding speed, (c) moderate heat input and welding speed, (d) sufficient heat input and slow welding speed.

content will be reduced after the melted wire is diluted by liquid base metals. Figure 18 shows that the ΔH values of Fe-Si and Ti-Si systems are far lower than that of Fe-Ti and Cu-Ti systems when the Si content is lower than 5 pct. Meanwhile, the ΔH of Fe-Ti is lower than that of Cu-Ti system. The results suggest that the reaction between the Fe and Ti atoms prefers to occur first in the molten pool. Referring the Cu-Fe-Ti phase diagram,^[23,24] the Fe_2Ti forms first at the temperature of 1773 K (1500 °C), and subsequently, the Si atoms enter into the Fe_2Ti lattices and substitute the Fe atoms to form the IMC of $\text{Fe}_{67-x}\text{Si}_x\text{Ti}_{33}$. With prolonging the solidification time and increasing contents of Fe and Ti *via* increasing the heat input, the volume fraction of $\text{Fe}_{67-x}\text{Si}_x\text{Ti}_{33}$ increases gradually. Meanwhile, the shape of $\text{Fe}_{67-x}\text{Si}_x\text{Ti}_{33}$ grows from the particle to the worm shape and dendrite in sequence, while the large-scale planar Cu matrix disappears gradually, as shown in Figures 7(e), 6(g), and 4(g).

Because the two main elements of Fe and Cu do not react with each other, the 316SS/FZ interface of all joints keeps as the 316SS. For the FZ/Ti6Al4V interface, Ti and Cu are the main elements. During welding, the

CuTi or CuTi_2 layer could be formed here by the reaction between dissolved Ti and melted Cu in the molten pool. Therefore, the FZ/Ti6Al4V interface close to the molten pool with a large volume fraction of liquid 316SS and Ti6Al4V would be a CuTi_2 layer due to the lower Cu content, while the FZ/Ti6Al4V interface close to the molten pool with a small volume fraction of liquid 316SS would form a CuTi layer due to the higher Cu content.

V. CONCLUSIONS

1. Laser-cold metal transfer arc hybrid welding with Cu3Si wire was employed to join dissimilar Ti6Al4V alloy and AISI316 stainless steel. The accepted joint with a cross-weld tensile strength up to 212 MPa was obtained under appropriate parameters.
2. The microstructures of the FZ and the interfaces within one joint are nonuniform from the top to the bottom but could become homogeneous by increasing heat input. The volume fraction of the

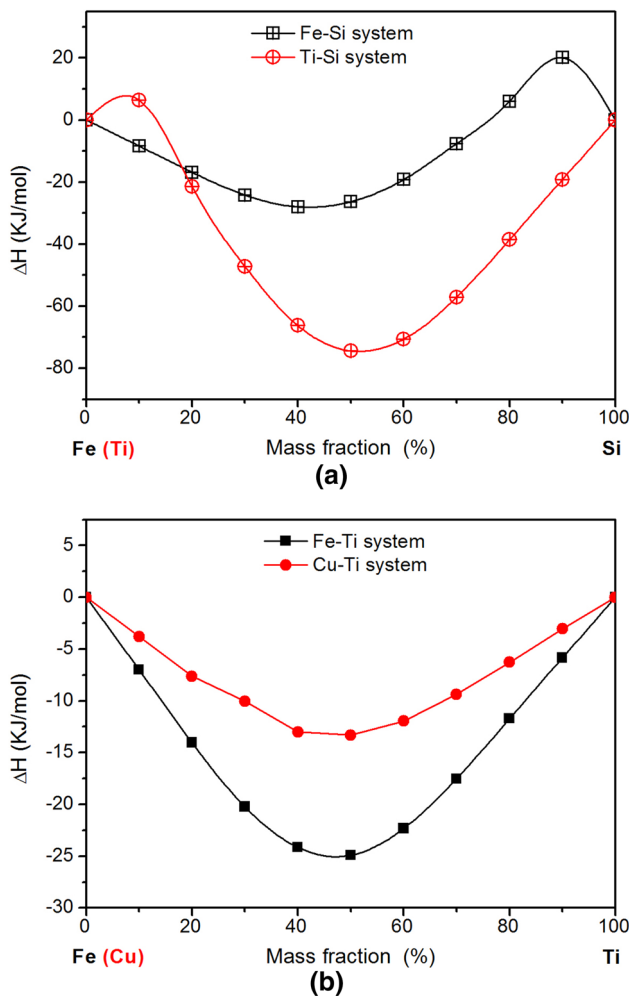


Fig. 18—Formation enthalpy, ΔH as a function of mass fraction calculated by Miedema model,^[30,31] (a) Fe-Si and Ti-Si system, (b) Fe-Ti and Cu-Ti system.

$\text{Fe}_{67-x}\text{Si}_x\text{Ti}_{33}$ in the FZ increases with the increase of heat input, and meanwhile, its shape varies from particles to worm-shape sticks and dendrites gradually. For the homogeneous joint, the FZ is represented by $\text{Fe}_{67-x}\text{Si}_x\text{Ti}_{33}$ dendrites spreading on the α -Cu matrix, and the two interfaces of 316SS/FZ and FZ/Ti6Al4V are characterized by a bamboo-like 316SS layer and a CuTi_2 layer, respectively.

- The tensile strength increases with the increase of heat input because the joint becomes more homogeneous. All tensile samples fractured at the CuTi_2 layer of Ti6Al4V side which is the hardest area of the joint. The fracture surfaces of both the Ti6Al4V side and the 316SS side are characterized by river pattern revealing brittle cleavage fracture.
- The microstructure differences between the joints and within one joint are attributed to the solidification rate decided by the heat input and the melt flow which is driven by arc pressure, surface tension along the laser keyhole, and the buoyancy results

from the density difference between melted Cu wire and base metals.

- Thermodynamic calculation demonstrates that the $\text{Fe}_{67-x}\text{Si}_x\text{Ti}_{33}$ is formed first in the molten pool of Cu-Fe-Si-Ti quaternary system, which causes the FZ is mainly composed of $\text{Fe}_{67-x}\text{Si}_x\text{Ti}_{33}$ and α -Cu.

REFERENCES

- A.E.L. Refaey and W. Tillmann: *Weld. J.*, 2008, vol. 87, pp. 113–18.
- G. Thirunavukarasu, S. Kundu, B. Mishra, and S. Chatterjee: *Metall. Mater. Trans. A*, 2014, vol. 45A, pp. 2067–77.
- A.E.L. Refaey and W. Tillmann: *J. Mater. Process. Technol.*, 2009, vol. 209, pp. 2746–52.
- M. Ghosh, S. Kundu, S. Chatterjee, and B. Mishra: *Metall. Mater. Trans. A*, 2005, vol. 36A, pp. 1891–99.
- S. Kundu, M. Ghosh, A. Laik, K. Bhanumathy, G.B. Kale, and S. Chatterjee: *Mater. Sci. Eng., A*, 2005, vol. 407, pp. 154–60.
- E. Atasoy and N. Kahraman: *Mater. Charact.*, 2008, vol. 59, pp. 1481–89.
- S. Kundu and S. Chatterjee: *Mater. Charact.*, 2008, vol. 59, pp. 631–37.
- S. Chen, J. Huang, K. Ma, X. Zhao, and A. Vivek: *Metall. Mater. Trans. A*, 2014, vol. 45A, pp. 3064–73.
- P. He, H. Yue, and J.H. Zhan: *Mater. Sci. Eng. A*, 2008, vol. 486, pp. 171–76.
- M. Gao, S.W. Mei, Z.M. Wang, X.Y. Li, and X.Y. Zeng: *Sci. Technol. Weld. Join.*, 2012, vol. 17, pp. 269–76.
- T. Wang, B.G. Zhang, G.Q. Chen, J.C. Feng, and Q. Tang: *Trans. Nonferrous Met. Soc. Chin.*, 2010, vol. 20, pp. 1829–34.
- H.C. Dey, M. Ashfaq, A.K. Bhaduri, and K. Prasad Rao: *J. Mater. Process. Tech.*, 2009, vol. 209, pp. 5862–70.
- M. Fazel-Najafabadi, S.F. Kashani-Bozorg, and A. Zarei-Hanzaki: *Mater. Des.*, 2010, vol. 31, pp. 4800–07.
- L.Q. Li, C.W. Tan, Y.B. Chen, W. Guo, and X.B. Hu: *Metall. Mater. Trans. A*, 2012, vol. 43A, pp. 4740–54.
- M. Gao, Z.M. Wang, X.Y. Li, and X.Y. Zeng: *Metall. Mater. Trans. A*, 2012, vol. 43A, pp. 163–72.
- S.H. Chen, L.Q. Li, Y.B. Chen, and J. Dai: *Mater. Des.*, 2011, vol. 32, pp. 4408–16.
- M. Gao, C. Chen, Y. Gu, and X.Y. Zeng: *Materials*, 2014, vol. 7, pp. 1590–1602.
- S. Chen, J. Huang, K. Ma, H. Zhang, and X. Zhao: *Metall. Mater. Trans. A*, 2014, vol. 44A, pp. 3690–96.
- S.W. Mei, M. Gao, J. Yan, C. Zhang, G. Li, and X.Y. Zeng: *Sci. Technol. Weld. Join.*, 2013, vol. 18, pp. 293–300.
- C. Bagger and F.O. Olsen: *J. Laser Appl.*, 2005, vol. 17, pp. 2–14.
- L.M. Liu, H.Y. Wang, and Z.D. Zhang: *Scripta Mater.*, 2007, vol. 56, pp. 473–76.
- X.D. Qi and G. Song: *Mater. Des.*, 2010, vol. 31, pp. 605–09.
- V. Raghvan: *J. Phase Equilib. Diff.*, 2002, vol. 23, pp. 172–74.
- J.A. Van Beek, A.A. Kodentsov, and F.J. Van Loo: *J. Alloys Compd.*, 1995, vol. 217, pp. 97–103.
- G. Effenberg and S. Ilyenko: in *Light Metal Ternary Systems: Phase Diagrams, Crystallographic and Thermodynamic Data*, 1st ed., Materials Science International Team MIST, Stuttgart, Germany, 2006, vol. 11A4, pp. 284–98.
- V. Raghvan: *J. Phase Equilib. Diff.*, 2009, vol. 30, pp. 393–96.
- F. Weitzer, J.C. Schuster, M. Naka, F. Stein, and M. Palm: *Intermetallics*, 2008, vol. 16, pp. 273–82.
- M. Gao, S.W. Mei, Z.M. Wang, X.Y. Li, and X.Y. Zeng: *J. Mater. Process. Technol.*, 2012, vol. 212, pp. 1338–46.
- J. Zhou and H.L. Tsai: *Int. J. Heat. Mass Trans.*, 2008, vol. 51, pp. 4353–66.
- A.R. Miedema, P.F. De Chatel, and F.R. De Boen: *Phys. B*, 1980, vol. 100, pp. 1–28.
- R.H. Davies, A.T. Dinsdale, and J.A. Gisby: *CALPHAD*, 2002, vol. 26, pp. 229–71.